Available online at www.sciencedirect.com
SCIENCE DIRECT®
Advances in Water Resources 29 (2006) 227–238
Advances in Water Resources
www.elsevier.com/locate/advwatres

Pore-scale characteristics of multiphase flow in porous media: A comparison of air–water and oil–water experiments

K.A. Culligan [a], D. Wildenschild [b,c,*], B.S.B. Christensen [c], W.G. Gray [d], M.L. Rivers [e]

[a] Department of Civil Engineering and Geological Sciences, University of Notre Dame, Notre Dame, IN 46556, USA
[b] Department of Geosciences, Department of Civil, Construction, and Environmental Engineering, Oregon State University, Corvallis, OR 97331, USA
[c] Environment and Resources, Technical University of Denmark, DK-2800 Lyngby, Denmark
[d] Department of Environmental Sciences and Engineering, University of North Carolina, Chapel Hill, NC 27599-7431, USA
[e] Consortium for Advanced Radiation Sources and Department of Geophysical Sciences, University of Chicago, IL, USA

Received 8 February 2005; accepted 11 March 2005
Available online 12 July 2005

Abstract

Studies of NAPL dissolution in porous media have demonstrated that measurement of saturation alone is insufficient to describe the rate of dissolution. Quantification of the NAPL–water interfacial area provides a measure of the expected area available for mass transfer and will likely be a primary determinant of NAPL removal efficiency. To measure the interfacial area, we have used a synchrotron-based CMT technique to obtain high-resolution 3D images of flow in a Soltrol–water–glass bead system. The interfacial area is found to increase as the wetting phase saturation decreases, reach a maximum, and then decrease as the wetting phase saturation goes to zero. These results are compared to previous findings for an air–water–glass bead study; The Soltrol–water interfacial areas were found to peak at similar saturations as those measured for the air–water system (20–35% saturation range), however, the peak values were in some cases almost twice as high for the oil-water system. We believe that the observed differences between the air–water and oil–water systems to a large degree can be explained by the differences in interfacial tensions for the two systems.

Keywords: Multi-phase flow; NAPLs; Porous media; Microtomography; Interfacial areas; Capillary pressure–saturation curves

1. Introduction

Understanding of multiphase flow, transport, and reaction processes in porous media is of critical importance to problems of groundwater supply and remediation, agricultural irrigation, and oil and gas recovery. However, lack of information about the microscale geometry and the microscale processes that control large-scale processes limits our ability to fully simulate multiphase problems. On the other hand, solution of field scale problems with a microscale level of detail is impractical, if not impossible. Thus, physical processes of interest must be described at larger length scales, a scale referred to here as the macroscale or Darcy scale. At this scale, rather than being adjacent, as at the microscale, different phases in a porous medium are described as overlapping continua, each occupying a fraction of space at a point [1]. This means that some variables, such as saturation and porosity, may be defined at the macroscopic level that have no meaning at the

* Corresponding author.
E-mail addresses: kculliga@nd.edu (K.A. Culligan), wildend@geo.oregonstate.edu (D. Wildenschild), brc@er.dtu.dk (B.S.B. Christensen), graywg@unc.edu (W.G. Gray), rivers@cars.uchicago.edu (M.L. Rivers).

0309-1708/$ - see front matter © 2005 Elsevier Ltd. All rights reserved.
doi:10.1016/j.advwatres.2005.03.021

microscale. However, some processes that occur, such as is the case for dissolution of non-aqueous phase liquids (NAPLs), cannot be fully described by macroscale variables alone. The wetting–non-wetting interfacial area has a large degree of influence on the mass transfer between the NAPL and the wetting fluid and therefore it is a controlling factor in dissolution of the NAPL. Based on this observation, measurement of microscale quantities such as interfacial areas are necessary complements to traditional macroscale measurements. In an effort to obtain microscale information, a number of researchers have used X-ray computed microtomography (CMT) to characterize the microscale structure of porous media [2–6].

Synchrotron-based computed microtomography is a non-destructive tool that can be used to investigate porous media and characterize microscale pore geometry. In general, medical computed tomography (CT) scanners have been employed because of their availability and relative ease of use. However, as interest in pore-scale characterization of porous media has increased, tools such as synchrotron-based X-rays, while limited in availability, have gained in popularity. Wildenschild et al. [4], for instance, demonstrated that the resolutions that can be obtained using CMT are much greater (5–20 μm) than those that can generally be obtained using more conventional and accessible CT techniques. Deriving quantitative information from images obtained with synchrotron-based CMT is also easier because of the absence of beam-hardening effects for the monochromatic synchrotron radiation.

Recent applications of CMT include its use to describe the complex pore space in network and pore-scale simulation models [7–9] as well as its use to support thermodynamic relationships developed in Gray et al. [10] that included the fluid–fluid interfacial area in the functional dependence of the capillary pressure [6]. Immiscible fluid flow applications include the study by Auzerais et al. [2] in which they used CMT to image the microstructure of Fontainebleu sandstone at a resolution of 7.5 μm per voxel.[1] They compared their experimental results to theoretical calculations made using a range of numerical techniques, including the lattice-gas method. They found good agreement between measured and calculated values for porosity, pore-volume-to-surface ratio, permeability, and end point relative permeability. Coles et al. [3] imaged a 6 mm subsection of a 2.54 cm diameter sandstone core sample at a resolution of 30 μm per voxel both prior to and immediately after flooding to residual oil saturation. The rock matrix images were used as input to both a pore network model and a Lattice Boltzmann simulator, and the end point saturation results were compared to the experimental images. Qualitative agreement was found between the experimental images and the simulated results. Culligan et al. [6] used the Advanced Photon Source (APS) to study unsaturated air–water flow through glass beads. A 5 mm subsection of a sample that was 7 mm in internal diameter and 7 cm tall was imaged. Images were taken over a range of saturations, and simultaneous capillary pressure measurements were made. A number of image processing techniques were used on the data collected to measure the wetting–non-wetting interfacial area. The interfacial area was found to increase as the saturation decreased, reach a maximum in the 20–35% saturation range, and continue to decrease as the saturation went toward zero. These findings were in agreement with a number of numerical studies reported in the literature (e.g. [11–13]).

Although air–water systems are predominant in natural multiphase flow problems, the flow and interaction of water with NAPL is a problem of continued interest. Modern groundwater contamination incidents often begin with the release of a NAPL into the subsurface. Once in the subsurface, the NAPL resides in the vadose zone or the saturated zone as a trapped residual immiscible phase. Determination of a remediation strategy depends upon appropriate characterization of the contaminated site. Studies of NAPL dissolution in porous media have demonstrated that the measurement of saturation alone is insufficient for describing the rate of NAPL dissolution (e.g. [14–17]). The wetting–non-wetting interfacial area provides a measure of the expected contact with the flushing solutions. It impacts the rate of transfer of NAPL into a flushing agent and will likely be a primary determinant of NAPL removal efficiency [18].

A number of researchers have used interfacial tracer techniques to measure the amount of wetting–non-wetting interfacial area available in NAPL–water systems (e.g. [19,18,20–23]). Most of these interfacial tracer studies have suggested that the interfacial area approaches a value just above the total solid phase interfacial area close to zero saturation, however our findings in Culligan et al. [6] did not support this, possibly because we were unable to image contributions from thin films[2] with the microtomography technique at the resolution used. A more likely reason, however, is that water held as films, i.e., water that is not controlled by capillary forces, is not expected to achieve thicknesses beyond tens of nanometers for smooth glass beads [24–27]. To further explore NAPL–water interaction in the subsurface, the present study presents LNAPL–water data collected using the synchrotron-based CMT technique and compares data to some of the air–water data presented in Culligan et al. [6]. Additionally, data is presented that

[1] A three-dimensional equivalent of a pixel.

[2] Wetting fluid that is not controlled by capillary forces and for which the thickness on glass beads likely is below the detection limit of the imaging system at the resolution used.

describes the fraction of the solid surface that is in contact with the wetting fluid. The objective of this paper is to understand better the differences between the air–water and oil–water experiments: Are the observed differences caused by the differences in interfacial tensions for the two systems?, by wettability issues? or perhaps by small differences in the experimental setup?

2. Methods and materials

2.1. Synchrotron X-ray computed microtomography

The experiments presented here were conducted at the GeoSoilEnviroCARS[3] (GSECARS) Bending Magnet Beamline (Sector 13 at the Advanced Photon Source, Argonne National Laboratory) and were performed using the same experimental setup as that used to collect the three-dimensional air–water images described in Culligan et al. [6]. During our use of the facility for the air–water experiments, the beam was run in fill-on-fill mode, with current ranging from 60 to 100 mA. For the oil–water experiments, the beam was run in top-up mode, which is a steady 100 mA, however, corrections made during the mathematical reconstruction eliminates variability in the calculated voxel values due to beam mode. As described in Wildenschild et al. [4], the beam is collimated from a fan beam to a parallel beam 50 mm wide and 5 mm high. A monochromator (Si(1 1 1)) is used to decompose the white synchrotron light to customized wavelengths in the energy range from 8 to 45 keV. This makes it possible to enhance the contrast between phases by selecting and scanning at the peak photoelectric absorption energy of an added chemical dopant. The monochromatic X-rays pass through the sample, are converted to visible light with a synthetic garnet (YAG) scintillator, and are imaged on a MicroMAX, 5 MHz, CCD Camera. The stage on which the sample is mounted is computer-automated to translate and rotate in the beam. A full rotation is 180° in 0.5° or 0.25° steps during which a number of flat fields (typically 25 or 50 angles apart) are taken, where the sample is moved out of the field of view, and a baseline intensity map is acquired. This information is used in the reconstruction of the data to correct for beam intensity decay, non-uniformities in the incident X-ray beam, and non-uniform responses of the scintillator and CCD camera. The camera dark current is also measured and used with the flat field to normalize each frame such that the full range of complete to zero absorption corresponds with an intensity range between 0.0 and 1.0. Reconstruction of the images was done with a filtered back-projection algorithm using code written in IDL™ (Research Systems Inc.) by Rivers (2003, the online tutorial) [28].

2.2. Experimental setup

For both the oil–water (OW) and air–water (AW) experiments, we used soda lime glass beads [6] with a bead density of 2.50 g/cm^3. They consisted of 35% (by weight) beads with 0.600 mm diameter, 35% of beads with 0.850 mm diameter, and 30% with bead diameter ranging from 1.0 to 1.4 mm. The glass beads were loosely packed in an acrylic sample tube for the AW experiments, whereas the beads were sintered first for the OW experiments, before packed in the acrylic tube. Both the soda lime glass beads and acrylic tube were preferentially water wet. In both the AW and OW experiments, the porosity was 34%, as computed from the number of air-filled pixels in the dry image. The water used to saturate the sample was doped with KI (1:6 KI:H_2O mass ratio), to enhance the contrast between the wetting and non-wetting phases. An energy level of 33.3 keV, slightly above the peak photoelectric absorption energy for iodide, was used for sample scanning. The sample was rotated twice through 180° in 1.0° increments, offset by 0.5° between the two passes, thereby resulting in 360 angles and an effective angle spacing of 0.5° for the AW experiments. A similar rotation was employed for the OW experiments, except that 0.5° increments were used, resulting in 0.25° final angle increments and 720 frames. Rotating the sample twice and offsetting the frames allowed for determination of possible bead movement between passes. The resulting voxel size was 17 μm for both the AW and OW experiments. Fig. 1 shows a three-dimensional rendering of a sample image.

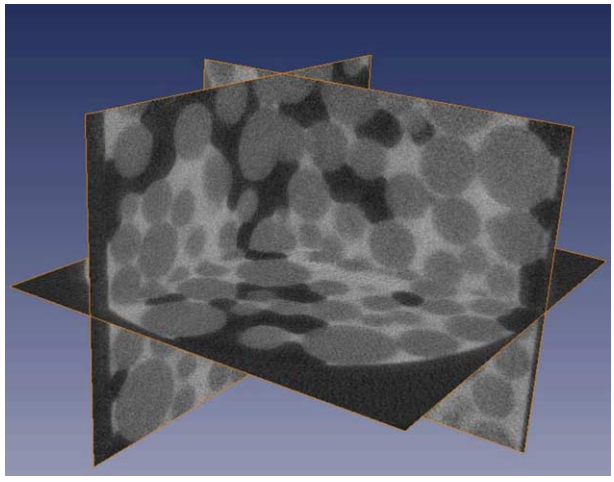

Fig. 1. Three-dimensional rendering of an AW data set. White (or light gray) illustrates regions of maximum attenuation (wetting-phase), black represents low attenuation (non-wetting phase), and the gray regions represent glass beads.

[3] CARS: Consortium for Advanced Radiation Sources.

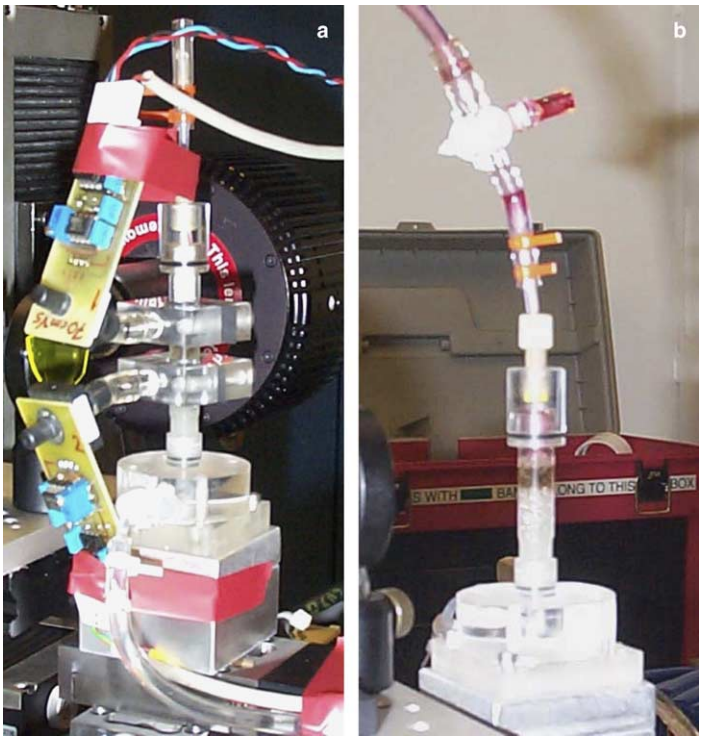

Fig. 2. (a) Experimental setup for the air–water experiments. A 5 mm vertical section between the two transducers was imaged. (b) Experimental setup for the oil–water experiments. The top of the sample was connected to an oil reservoir.

2.2.1. Air–water experiments

As reported in Culligan et al. [6], the acrylic column used for the loosely packed glass bead experiments was 7.0 cm in height with an internal diameter of 7.0 mm. The sample tube is presented in Fig. 2a (see also [5,6]). Images were taken of a 5 mm vertical interior section of the sample tube (between the two pressure transducers shown in Fig. 2a). The sample was packed dry above a porous nylon membrane (1.2 μm MAGNA filter from Osmonics Inc.). This semi-permeable membrane is permeable only to the wetting phase, and separates the wetting phase reservoir from the bead pack. The top of the sample was open to the atmosphere. The wetting phase reservoir was connected to a Harvard Apparatus, Inc., Model 44, programmable, electronic, syringe pump. The sample was saturated by a primary imbibition and drainage loop at a flow rate of 0.25 ml/h (1.8×10^{-4} cm/s, Capillary number, $Ca = 0.2643 \times 10^{-7}$). Secondary imbibition and drainage took place at a flow rate of 0.25 ml/h (1.8×10^{-4} cm/s, $Ca = 0.2643 \times 10^{-7}$), while the third imbibition and drainage loop rate was 2.0 ml/h (1.4×10^{-3} cm/s, $Ca = 0.2055 \times 10^{-7}$). From, preliminary laboratory experiments it was concluded that this range of flow rates resulted in quasi-static capillary pressure–saturation curves for both the AW and OW experiments (i.e., conditions that approximate hydrostatic equilibrium). An overview of the experimental details is presented in Table 1. The starting point of the drainage cycle was defined as the time when the capillary pressure in the sample reached a minimum value of 0.0 cm. Before scanning the sample, the pump was stopped at regular intervals, corresponding to acquisition of 10–12 evenly distributed points on the capillary pressure–saturation curve. After the pump was stopped, the fluids were allowed to redistribute for 10 min and a 10-min scan was taken. In addition to the two pressure transducers shown in Fig. 2a, a pressure transducer was located in the wetting phase reservoir from which capillary pressure readings were taken every 2 s. It was this pressure reading that was used for the capillary pressure curves.

Table 1
Experimental settings

	Experiment	Flow rate
Air–water	Primary imbibition and drainage	0.25 ml/h, 1.8×10^{-4} cm/s
	Secondary imbibition and drainage	0.25 ml/h, 1.8×10^{-4} cm/s
	Third imbibition and drainage	2.0 ml/h, 1.4×10^{-3} cm/s
Oil–water	Primary imbibition and drainage (not imaged)	0.5 ml/h, 3.6×10^{-4} cm/s
	Secondary imbibition and drainage	0.5 ml/h, 3.6×10^{-4} cm/s
	Third imbibition and drainage	3.0 ml/h, 2.2×10^{-3} cm/s

2.2.2. Oil–water experiments

The sample used for the OW experiments consisted of a sintered 4.0 cm high and, 7.0 mm OD column, placed inside a 7.0 cm tall cylinder. The glass beads were sintered in a 7.0 mm internal diameter graphite crucible at 740 °C for 30 min. Once cooled the sintered core was placed in the tight-fitting acrylic sample holder. A porous nylon membrane separated the sintered bead pack from the wetting phase reservoir. The wetting phase reservoir was connected to a Precision Instruments SP210IW, programmable, electronic, syringe pump. The top of the sample was connected to a static oil reservoir. The oil used in the experiments was Soltrol 220 (Chevron Phillips, $\rho = 0.803$ g/cm^3 at 15.6 °C, which is negligibly soluble in water), dyed red (Fig. 2b) with Oil Red O (Sigma Aldrich). The sample was initially dry, from which point a primary imbibition curve was run at a flow rate of 0.50 ml/h (3.6×10^{-4} cm/s, $Ca = 0.9890 \times 10^{-7}$). The oil phase reservoir was then connected at the top of the sample, and primary drainage was run, again at a flow rate of 0.50 ml/h (3.6×10^{-4} cm/s, $Ca = 0.9890 \times 10^{-7}$). Secondary imbibition and drainage were run at a flow rate of 0.50 ml/h (3.6×10^{-4} cm/s, $Ca = 0.9890 \times 10^{-7}$). The flow rate for the third imbibition and drainage cycle was 3.0 ml/h (2.2×10^{-3} cm/s, $Ca = 0.6044 \times 10^{-6}$). Again, the pump was stopped, the fluids were allowed to equilibrate for 10 min and scanned. Due to changes in the way the computer interfaced with the camera and the number of angles being collected, the imaging time increased to an average of 30 min.

Imbibition was stopped after the water rose to the top of the 4.0 cm tall glass bead column. At this point, the flow direction of the pump was reversed to initiate drainage. This was done so that the water would not enter the oil tubing leading to the oil reservoir.

2.2.3. Image analysis

The original gray scale data were segmented using cluster analysis and median filtering [29], to separate the beads, wetting and non-wetting phases. A subset of the segmented image was cropped from the total image to minimize the possible effects of wall flow. All subsequent image analyses were conducted using the cropped subset. Saturations were determined as described in Wildenschild et al. [29]. The number of voxels of wetting and non-wetting phase were counted, so that the wetting phase saturation could be determined.

Interfacial area was computed using the commercial image analysis program, Amira™ [6]. The program uses a modified marching cubes algorithm to generate isosurfaces to represent a desired surface. The wetting–non-wetting interfacial area a^{wn} (excluding the presence of films, since they were not resolved) can then be determined according to:

$$a^{wn} = \frac{1}{2}(a^{w} + a^{n} - a^{s}), \tag{1}$$

where a^{w} is the total wetting phase interfacial area, a^{n} is the total non-wetting phase interfacial area, and a^{s} is the total solid phase interfacial area. The wetted fraction of the solid surface, x_s^{ws}, was computed from:

$$x_s^{ws} = a^{w} - a^{wn}. \tag{2}$$

An REV analysis [6] demonstrated that the interior-segmented section was larger than the required REV for saturation and interfacial area computations for all collected data. The average grain size for the AW experiments was 0.8675 mm, corresponding to average number of grain diameters in the x, y, and z directions of 5.2, 5.9, and 5.7, respectively, for the interior imaged section. REV analysis within this section showed that the error on the wetting–non-wetting interfacial area values and saturation values varied only 5% and 0.5%, respectively. Thus, the imaging volume was represented adequately.

3. Results

Tables including all of the data presented in the results section are not included in this manuscript, but can be obtained by contacting the corresponding author.

3.1. Capillary pressure–saturation curves

Capillary pressure–saturation curves obtained during the course of the AW and OW experiments are presented in Fig. 3. The capillary pressure measurements were adjusted, so that the measured water pressure was zero when the water surface was level with the top of the glass bead pack. The entry pressure for the AW experiments is approximately 4.3 cm, while the entry pressure for the OW experiments is much lower and

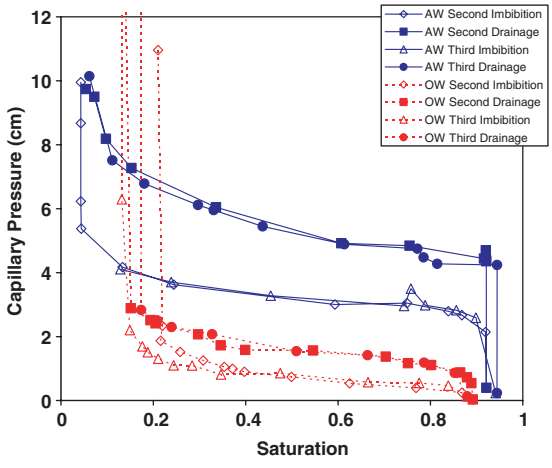

Fig. 3. Capillary pressure–saturation curves for AW (solid blue) and OW (dashed red) experiments. Open and closed symbols designate imbibition and drainage curves, respectively.

not clearly defined. While the third imbibition and drainage loop for the AW and OW experiments were run at higher flow rates (2.0 ml/h and 3.0 ml/h, respectively) than the second loop, no rate effects in the capillary pressure–saturation curves were observed for either flow rate. As can be seen, the OW drainage curves are below the AW drainage curves. This is in accordance with the differences in interfacial tensions for the respective fluid pairs (0.0364 N/m for Soltrol 220 and water, and 0.0681 N/m for air and water). These results also agree with the Soltrol–water studies by Liu et al. [30], the dodecane–water, xylene–water, trichloroethane–water, and butyl acetate–water studies of Demond and Roberts [31], and the PCE–water study of Ferrand et al. [32]. Imbibition curves are less frequently measured, yet our results are consistent with the differences in interfacial tension for the involved fluid pairs and with the results of Demond and Roberts [31].

3.2. Saturation profiles

Figs. 4 and 5 compare the vertical (wetting phase) saturation profiles of both the AW and OW experiments for secondary imbibition and drainage, respectively. As can be seen in the figures, the AW experiments reach a slightly higher wetting phase saturation on imbibition (Fig. 4) than the OW experiments, attributed to the low residual air phase saturation and relatively high residual oil phase saturation in Fig. 3. An average residual wetting phase saturation of 5.0% was reached along the second AW drainage branch (Fig. 5), whereas an average value of 13.1% was measured along the second OW drainage branch. The sharp fronts of the AW drainage saturation profiles are an indication that the air phase is not fully connected across the sample. This is in contrast to the more uniform flow of the OW system, where oil phase connectivity is reached early in the drainage process. However, the AW drainage saturation profiles become more uniform at lower saturations, once air phase connectivity has been achieved. Because the oil remains behind at such high residual saturations in the OW experiments, oil phase connectivity is achieved very early on, resulting in a series of uniform saturation profiles. This result could also be caused by wall effects. Despite our efforts to create a tight fit of the sintered glass beads within the sample holder, it was not as good as for the loosely-packed bead sample. Nevertheless, wall effects in the resulting curves were minimized by considering only the center portion of the images in the data analyses. The reverse process was observed during imbibition (Fig. 4), where air phase connectivity is lost early on in the AW experiments, whereas the oil phase maintains connectivity and a uniform distribution during the OW experiments. Even in the presence of a wall effect, the water phase pressure continues to decrease due to the presence of the semi-permeable membrane at the bottom outlet, so that water continues to drain from the sample despite the presence of oil along the walls.

3.3. Wetting–non-wetting interfacial area

The wetting–non-wetting interfacial area, excluding fluid film interfaces, are shown as a function of wetting phase saturation in Fig. 6. A functional relationship

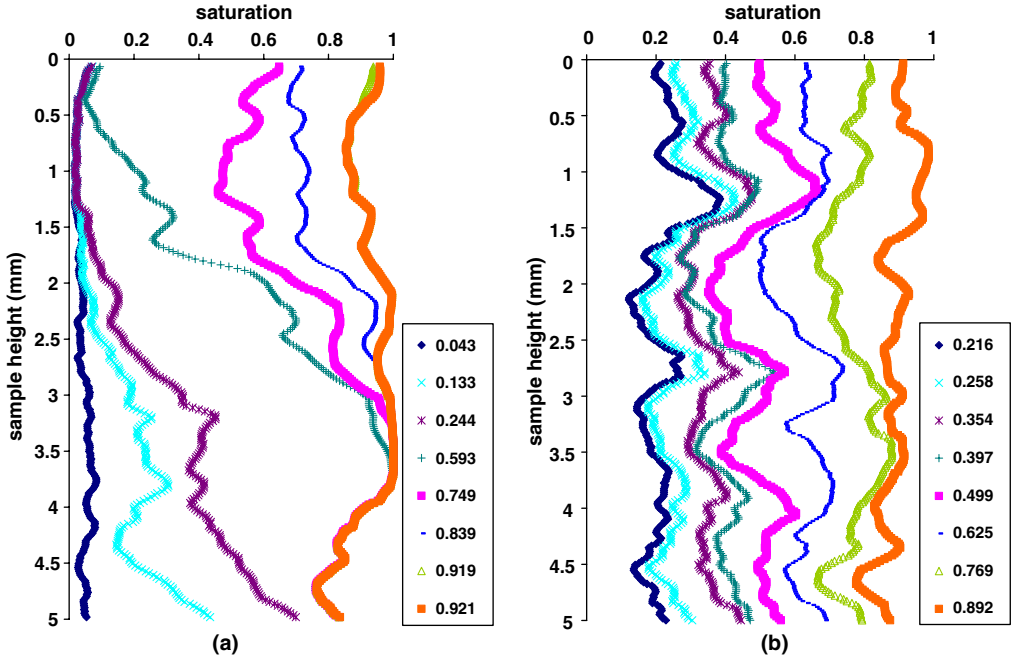

Fig. 4. Wetting phase saturation profiles for secondary imbibition: (a) air–water and (b) oil–water. The legends are average wetting phase saturations for the imaged region. Air/oil enters on top, water flows in/out through the bottom.

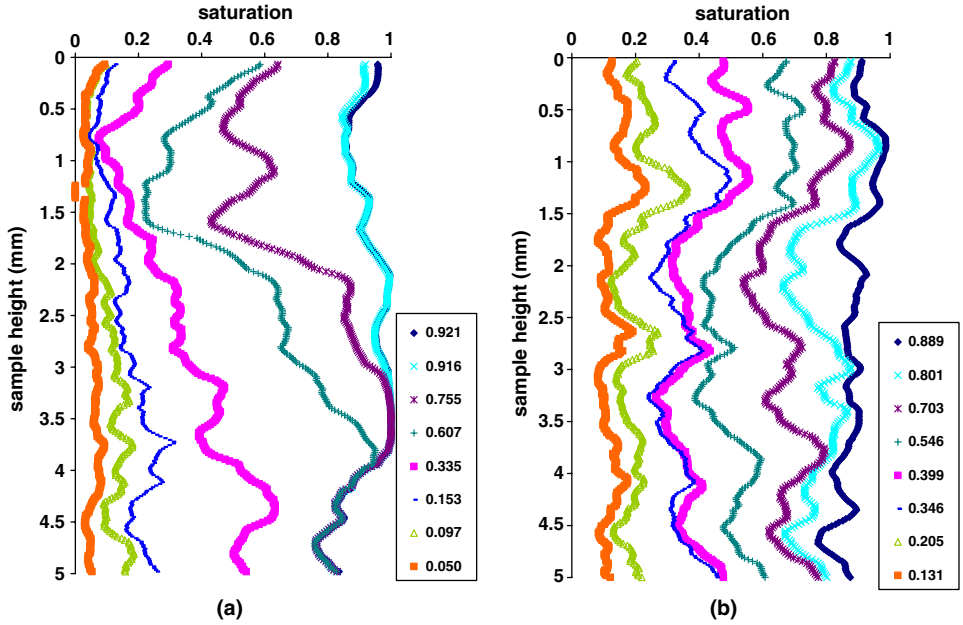

Fig. 5. Wetting phase saturation profiles for secondary drainage: (a) air–water and (b) oil–water. The legends are average wetting phase saturations for the imaged region. Air/oil enters on top, water flows in/out through the bottom.

among the wetting–non-wetting interfacial area, the wetting-solid interfacial area, the wetting phase saturation, and the capillary pressure was proposed in Hassanizadeh and Gray [33] and Gray et al. [10], where the capillary pressure–saturation relationship is hypothesized to be a two-dimensional projection of a complex, multidimensional surface. The projection of this surface onto a two-dimensional plane results in hysteresis of the capillary pressure–saturation relationship. The two-dimensional micromodel studies of Cheng et al. [34] demonstrated the validity of inclusion of the interfacial area as an independent variable in the capillary pressure

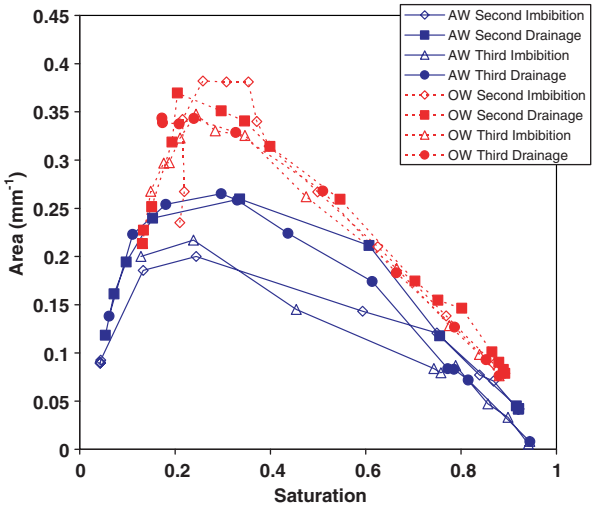

Fig. 6. Wetting–non-wetting interfacial area versus saturation for AW (solid blue) and OW (dashed red) experiments. Open and closed symbols designate imbibition and drainage curves, respectively.

functional dependence, thereby lifting the ambiguity associated with the hysteretic relationship between capillary pressure and saturation. In agreement with our study, the macroscopic theory of Hassanizadeh and Gray [33] predicts that, in the absence of films, the interfacial area will increase from zero towards a maximum, and decreases back to zero as the wetting phase saturation decreases. This model of interfacial area behavior as a function of saturation is supported by numerical modeling studies as well [11–13]. Our results show that the maximum interfacial area values of the AW experiments are larger for drainage than imbibition, as is expected if the simple capillary tube theory is assumed. Upon drainage, the fluid interface would be more stretched, as apposed to imbibition where the interface is expected to be flatter [6], as illustrated in Fig. 7. This simple hysteresis analysis does not hold for the OW results. The OW second imbibition points lie above the

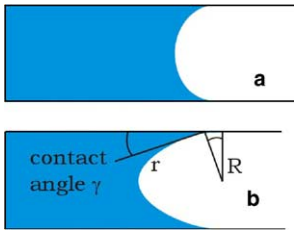

Fig. 7. (a) The interface in a capillary tube imbibing water is expected to be flatter than the interface in a capillary tube that is draining (b), resulting in less interfacial area. However, the contact points have not moved, and the wetted fraction of the solid surface is the same in both cases, meaning that the wetted fraction of the solid surface is a non-hysteretic function of saturation.

OW second drainage points in Fig. 6. This may be because the OW second imbibition curve crosses over the other capillary pressure–saturation curves at the low saturation end in Fig. 3.

The peak OW interfacial areas in Fig. 6 are higher than those observed for the AW experiments, yet the peaks occur in a similar saturation range of ~20–35%. As Fig. 8 shows, the oil is located in numerous smaller, more disconnected fluid configurations in the vicinity of these peak interfacial area values, whereas the air phase is configured in larger, but fewer and more continuous fluid configurations. This is the reason we observe higher peak interfacial areas for the OW system than for AW. The reason for the air to be in larger, more continuous fluid configurations is likely related to differences in interfacial tension. As mentioned previously, the interfacial tension between Soltrol 220 and water is 0.0364 N/m, while that between air and water is 0.0681 N/m. Recall that

$$p^{c} = \frac{2\sigma}{r}, \tag{3}$$

where p^{c} is the capillary pressure, σ is the interfacial tension, and r is the radius of curvature. This means that for a given capillary pressure:

$$r_{ow} < r_{aw}. \tag{4}$$

Therefore, the oil will distribute within the water such that its interfacial curvature will be larger than that of the AW interfaces. Such a distribution may be achieved if the oil exists in smaller fluid arrangements. Fig. 9 depicts fluid configurations for an ideal situation, in a system where there is no solid phase. The differences in fluid–fluid interfacial tensions cause the fluids to configure as illustrated in Fig. 9 where the higher interfacial tension (on the right) results in large bubbles of red fluid dispersed in the blue fluid, compared to the smaller and more numerous bubbles of red fluid for the lower interfacial tensions on the left.

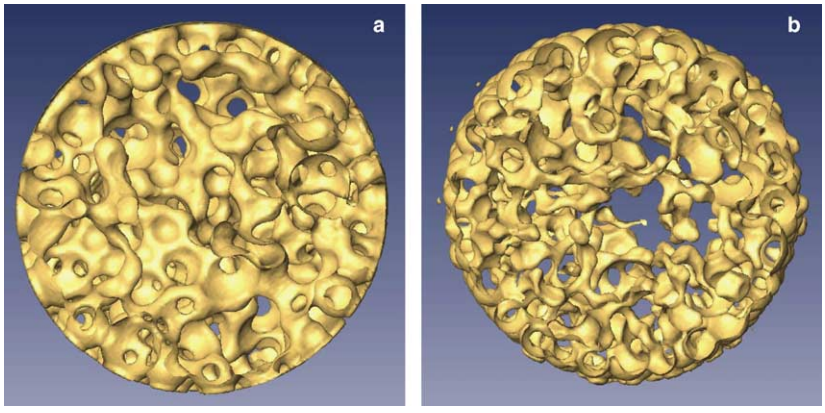

Fig. 8. Non-wetting phase distributions in three dimensions for the second imbibition branch. (a) The air phase is located in larger continuous fluid configurations at $s^{w} = 24.4\%$ compared to (b) the oil phase which is located in smaller and less well-connected configurations at a similar saturation: $s^{w} = 23.9\%$, leading to higher interfacial area values at these lower saturations.

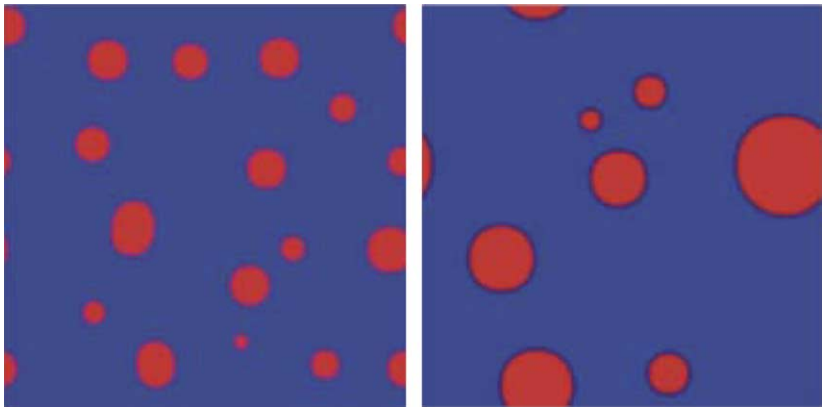

Fig. 9. Distribution and sizes of fluid configurations for two systems with different interfacial tension in the absence of a solid phase. The fluid–fluid interfacial tension is a factor of two higher on the right than on the left. The figures were generated with a Lattice–Boltzmann code and are courtesy of M.G. Schaap, UC Riverside.

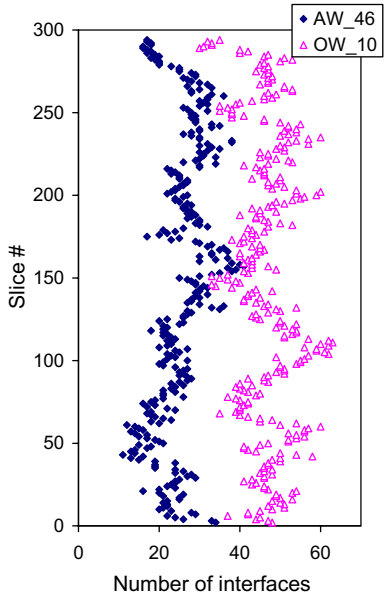

Fig. 10. The number of interfaces in a horizontal slice as a function of sample height for both AW and OW systems. The analysis was performed on the same volumes as illustrated in Fig. 8, near the peak interfacial area values for the second imbibition branch.

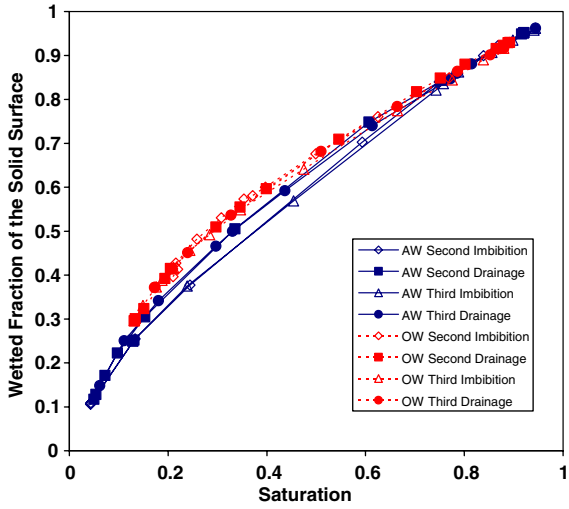

Fig. 11. Wetted fraction of the solid surface as a function of wetting phase saturation for AW (solid blue) and OW (dashed red) experiments. Open and closed symbols designate imbibition and drainage curves, respectively.

To support our hypothesis, we calculated the number of wetting–non-wetting interfaces in each horizontal slice of both the AW an OW systems (Fig. 10). Our analysis clearly supports the notion that air is located in fewer, but larger continuous fluid arrangements, while oil is located in smaller, more numerous and less well-connected fluid configurations.

3.4. Wetted fraction of the solid surface

The extended functional dependence for the capillary pressure included in the theory of Gray et al. [10] considers not only the wetting phase saturation, but also includes the wetting–non-wetting interfacial area, the wetting-solid interfacial area, and the solid phase interfacial area. The wetted fraction of the solid surface is a function of the wetting-solid interfacial area and the solid phase interfacial area. These wetted fractions can be calculated from the images, using Eq. (2). The wetted fraction of the solid surface is shown in Fig. 11 as a function of the wetting phase saturation. It is an almost non-hysteretic function of the wetting phase saturation, and similar for both AW and OW systems. Thus, for a system in which it can be assumed that the solid phase interfacial area is constant, this suggests that the wetting-solid interfacial area is known as a unique function of saturation. Therefore, it does not need to be included as an independent variable in the capillary pressure functional dependence of Gray et al. [10].

Fig. 12a and b, showing AW experimental results, at similar saturations of 13.3% and 11.1% for the imbibition and drainage branch, respectively, have almost the same wetted fractions of 0.255 and 0.251, yet have different fluid configurations. This can also be seen in the higher saturation range in Fig. 12c and d where the saturations are 74.9% and 77.2%, and the wetted fractions are 0.840 and 0.847 for the imbibition and drainage branch, respectively. These results are to be expected if we again consider the simple capillary tube model [6] shown in Fig. 7. Fig. 7a shows a capillary tube, just prior to imbibing water. The interface has flattened, but has not yet moved, and the interfacial area has decreased. Fig. 7b shows the same capillary, just prior to draining. The interface has stretched, thereby increasing the interfacial area. The wetted fraction of the solid surface, however, has not changed between these two different interface configurations. This phenomenon of contact angle hysteresis results in different fluid configurations for the same fluid saturation. It suggests that when using CMT measurements to validate numerical models, one should use caution and perhaps compare macroscale variables, obtained from microscale measurements, such as saturation and interfacial area.

4. Discussion and conclusion

While the dynamics of the air phase is generally neglected in AW experiments, this cannot be done in OW experiments. In capillary pressure–saturation measurements, it is assumed that the air phase pressure is everywhere at equilibrium with the atmosphere. The air is essentially an inviscid fluid whereas the oil is a viscous fluid flowing in conjunction with the water. This

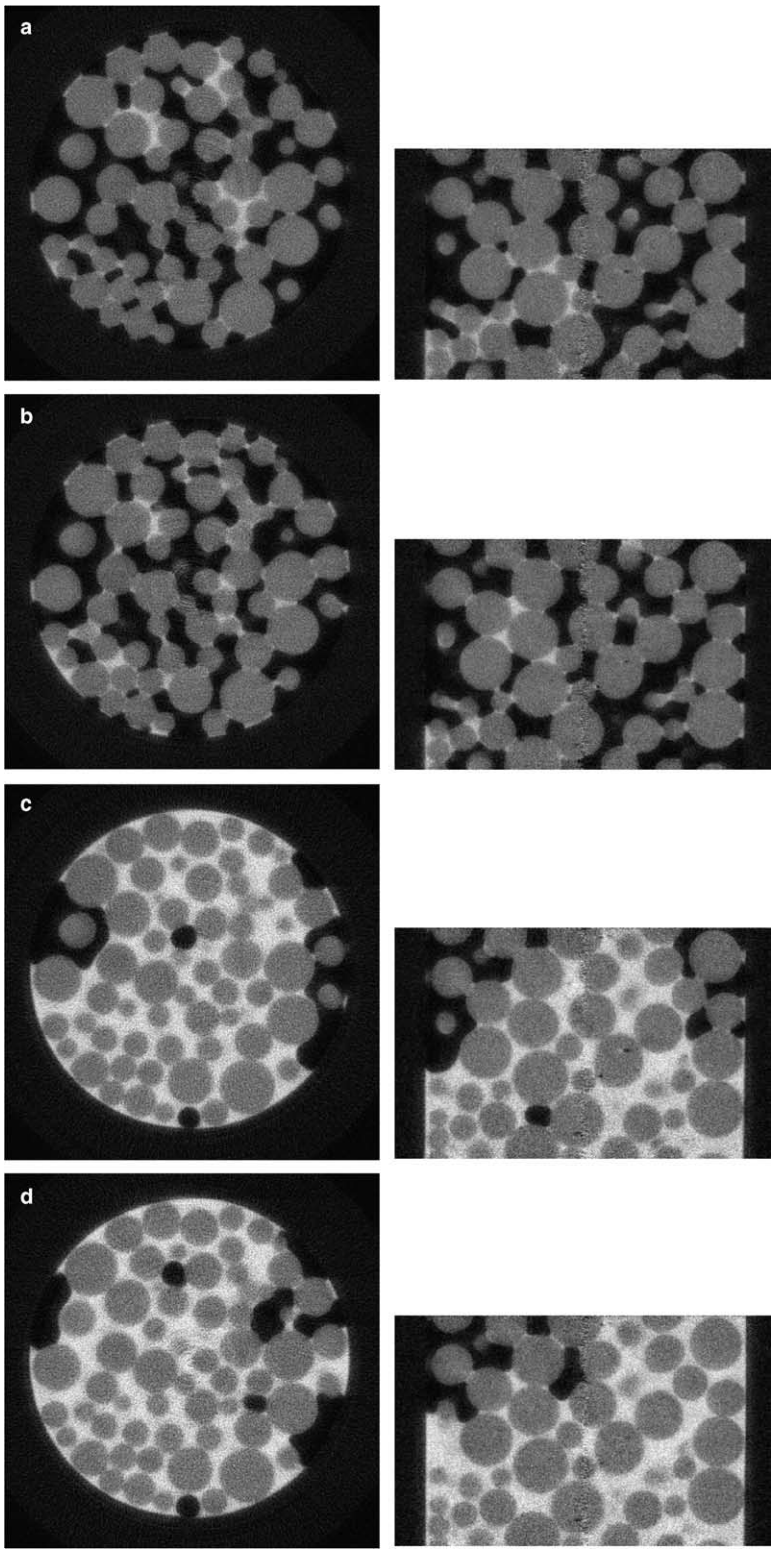

Fig. 12. (a) Horizontal and vertical cross-section of an AW volume ($s^w = 13.3\%$) along the second imbibition branch. (b) Horizontal and vertical cross-section of an AW volume ($s^w = 11.1\%$), along the third drainage branch. (c) Horizontal and vertical cross-section of an AW volume ($s^w = 74.9\%$), along the second imbibition branch. (d) Horizontal and vertical cross-section of an AW volume ($s^w = 77.2\%$), which is located on the third drainage branch.

could explain some of the observed differences between the AW and OW experiments. The more uniform saturation profiles along with the images illustrate that the oil phase connectivity is achieved much sooner than

the air phase connectivity during both drainage and imbibition. The higher observed residual oil saturation was apparent in the saturation profiles as well as the capillary pressure–saturation curves. The images showed that the residual oil in the OW experiments is arranged in smaller fluid configurations than the residual air phase in AW experiments, likely because of differences in interfacial tension between the fluid pairs. This leads to a higher interfacial area for the OW fluid pair.

Differences between the AW and OW experiments could also possibly be attributed to differences in the experimental setup. For instance, it was clear from the imaged fluid distribution profiles that some preferential flow occurred along the walls in the OW experiments, using sintered glass beads, that did not occur in the loosely packed AW experiments. We could not be sure how this affected the final results, however, we believe that effects were minimized by limiting our analyses to the cropped center section of the images.

Microscale experiments such as those presented here have useful macroscale results. For example, mass transfer processes such as NAPL dissolution are typically modeled using an effective rate constant that implicitly represents the combined effects of interfacial area and reaction rates, despite no knowledge of the specific interfacial area in the system [35]. Therefore, while not explicitly accounted for, interfaces are incorporated into mass transfer models. Thus, the specific interfacial area is an important macroscale variable. Incorporation of this parameter into transport models will be an important step in the development of robust simulators that correctly describe mass, momentum, and energy transfer between phases [6]. We have shown that the wetting–non-wetting interface can be an important variable, unlike the wetted fraction of the solid surface that may be neglected as an independent variable [10]. However, the results pertaining to the wetted fraction of the solid surface (Fig. 12) demonstrate that comparisons between macroscale experimental data (obtained from microscale measurements) and numerical simulations may potentially be more meaningful than direct microscale comparisons, for instance comparison of measured and simulated fluid geometries in a 2D slice (e.g. [3]).

We note that our results pertain to idealized porous systems of glass beads that do not necessarily hold for natural systems. Additional challenges must be over come to apply the CMT technique to natural systems. These include the effect of mineral heterogeneity on attenuation and the difficulty to resolve small-scale features such as small particles and films. Additional interesting questions that could be investigated using CMT include the physics of mixed wettability and three-phase flow systems. We are convinced that the synchrotron-based CMT technique will prove to be a very valuable research tool in the years to come.

Acknowledgements

This work was supported by a National Science Foundation (NSF) Graduate Research Fellowship, NSF grant DMS-0327896, NSF grant EAR-0337711, and a grant from the Danish Technical Research Council. WGG acknowledges partial support of his effort on this work by NSF through DMS-0112069 to the Statistical and Applied Mathematical Sciences Institute in Research Triangle Park. Portions of this work were performed at GeoSoilEnviroCARS (Sector 13), Advanced Photon Source (APS), Argonne National Laboratory. GeoSoilEnviroCARS is supported by the National Science Foundation—Earth Sciences (EAR-0217473), Department of Energy—Geosciences (DE-FG02-94ER14466) and the State of Illinois. Use of the APS was supported by the US Department of Energy, Basic Energy Sciences, Office of Energy Research, under Contract No. W-31-109-Eng-38. We thank the entire GSECARS staff for experimental assistance.

References

[1] Gray WG, Leijnse A, Kolar RL, Blain CA. Mathematical tools for changing spatial scales in the analysis of physical systems. Boca Raton: CRC Press; 1993.
[2] Auzerais FM, Dunsmuir J, Ferreol BB, Martys N, Olson J, Ramakrishnan TS, et al. Transport in sandstone: a study based on three dimensional microtomography. Geophys Res Lett 1996;23(7):705–8.
[3] Coles ME, Hazlett RD, Spanne P, Soll WE, Muegge EL, Jones KW. Pore level imaging of fluid transport using synchrotron X-ray microtomography. J Petrol Sci Eng 1998;19(1–2):55–63.
[4] Wildenschild D, Hopmans JW, Vaz CMP, Rivers ML, Rikard D. Using X-ray computed tomography in hydrology: systems, resolutions, and limitations. J Hydrol 2002;267(3–4):285–97.
[5] Wildenschild D, Hopmans JW, Kent AJR, Rivers ML. A quantitative study of flow-rate dependent processes using x-ray microtomography. Vadose Zone J 2005;4:112–26.
[6] Culligan KA, Wildenschild D, Christensen BSB, Gray WG, Tompson AFB. Interfacial area measurements for unsaturated flow through a porous medium. Water Resour Res 2004;40(12), in press.
[7] Ferreol B, Rothman DH. Lattice–Boltzmann simulations of flow through Fontainebleu sandstone. Transport Porous Media 1995;20(1–2):3–20.
[8] Hazlett RD, Chen SY, Soll WE. Wettability and rate effects on immiscible displacement: Lattice–Boltzmann simulation in microtomographic images of reservoir rocks. J Petrol Sci Eng 1998;20(3–4):167–75.
[9] Zhang D, Zhang R, Chen S, Soll WE. Pore scale study of flow in porous media: scale dependency, REV, and statistical REV. Geophys Res Lett 2000;27(8):1195–8.
[10] Gray WG, Tompson AFB, Soll WE. Closure conditions for two-fluid flow in porous media. Transport Porous Media 2002;47(1):29–65.
[11] Reeves PC, Celia MA. A functional relationship between capillary pressure, saturation, and interfacial area as revealed by a pore-scale network model. Water Resour Res 1996;32(8):2345–58.

[12] Berkowitz B, Hansen DP. A numerical study of the distribution of water in partially saturated porous rock. Transport Porous Media 2001;45(2):303–19.
[13] Dalla E, Hilpert M, Miller CT. Computation of the interfacial area for two-fluid porous medium systems. J Contam Hydrol 2002;56:25–48.
[14] Miller CT, Poirier-McNeill MM, Mayer AS. Dissolution of trapped nonaqueous phase liquids—mass transfer characteristics. Water Resour Res 1990;26(11):2783–96.
[15] Powers SE, Abriola LM, Weber WJ. An experimental investigation of nonaqueous phase liquid dissolution in saturated subsurface systems—steady-state mass transfer rates. Water Resour Res 1992;28(10):2691–705.
[16] Imhoff PT, Jaffe PR, Pinder GF. An experimental study of complete dissolution of a nonaqueous phase liquid in saturated porous media. Water Resour Res 1994;30(2):307–20.
[17] Nambi IM, Powers SE. NAPL dissolution in heterogeneous systems: an experimental investigation in a simple heterogeneous system. J Contam Hydrol 2000;44(2):161–84.
[18] Annable MD, Jawitz JW, Rao PSC, Dai DP, Kim H, Wood AL. Field evaluation of interfacial and partitioning tracers for characterization of effective NAPL–water contact areas. Ground Water 1998;36(3):495–503.
[19] Saripalli KP, Kim H, Rao PSC, Annable MD. Measurement of specific fluid–fluid interfacial areas of immiscible fluids in porous media. Environ Sci Technol 1997;31(3):932–6.
[20] Saripalli KP, Annable MD, Rao PSC. Estimation of non-aqueous phase liquid (NAPL)–water interfacial areas in porous media during chemical flooding. Environ Sci Technol 1997;31(12):3384–8.
[21] Saripalli KP, Rao PSC, Annable MD. Determination of specific NAPL–water interfacial areas of residual NAPLs in porous media using the interfacial tracer technique. J Contam Hydrol 1998;30(3–4):375–91.
[22] Schaefer CE, DiCarlo DA, Blunt MJ. Determination of water–oil interfacial area during 3-phase gravity drainage in porous media. J Colloid Interf Sci 2000;221(2):308–12.
[23] Dai DP, Barranco FT, Illangaskare TH. Partitioning and interfacial tracers for differentiating NAPL entrapment configuration: column-scale investigation. Environ Sci Technol 2001;35(24):4894–9.
[24] Dullien FAL. Porous media: fluid transport and pore structure. 2nd ed. San Diego: Academic Press; 1992.
[25] Pashley RM. Multilayer adsorption of water on silica: an analysis of experimental results. J Colloid Interf Sci 1980;78:246–8.
[26] Langmuir I. Repulsive forces between charged surfaces in water and the cause of Jones-Ray effect. Science 1938;88:430–2.
[27] Tokonaga T. Personal communication, 2004.
[28] Rivers ML. Tutorial introduction to X-ray computed microtomography data processing, 2003. Available from: <http://www-fp.mcs.anl.gov/xray-cmt/rivers/tutorial.html>.
[29] Wildenschild D, Culligan KA, Christensen BSB, Rivers ML, Joshi B. Estimating multi-phase pore-scale characteristics from X-ray tomographic data using cluster analysis-based segmentation, Vadose Zone J, in review.
[30] Liu YP, Hopmans JW, Grismer ME, Chen JY. Direct estimation of air–oil and oil–water capillary pressure and permeability relations from multi-step outflow experiments. J Contam Hydrol 1998;32(3–4):223–45.
[31] Demond AH, Roberts PV. Effect of interfacial forces on 2-phase capillary pressure–saturation relationships. Water Resour Res 1991;27(3):423–37.
[32] Ferrand LA, Milly PCD, Pinder GF, Turrin RP. A comparison of capillary-pressure saturation relations for drainage in 2-fluid and 3-fluid porous media. Adv Water Resour 1990;13(2):54–63.
[33] Hassanizadeh SM, Gray WG. Thermodynamic basis of capillary pressure in porous media. Water Resour Res 1993;29(10):3389–405.
[34] Cheng JT, Pyrak-Nolte LJ, Nolte DD, Giordano NJ. Linking pressure and saturation through interfacial areas in porous media. Geophys Res Lett 2004;31. doi:10.1029/2003GL019282.
[35] Johns ML, Gladden LF. Magnetic resonance imaging study of the dissolution kinetics of octanol in porous media. J Colloid Interf Sci 1999;210(2):261–70.